

Development and validation of a high-resolution hyperspectral imaging system for the retina

Minh H. Tran^{1,2}, Kelden Pruitt^{1,2}, Michelle Bryarly^{1,2}, Isioma Emordi^{1,2},
Arrsh Ali^{1,2}, Ling Ma^{1,2}, and Baowei Fei^{1,2,3,*}

¹University of Texas at Dallas, Department of Bioengineering, Richardson, Texas, United States

²University of Texas at Dallas, Center for Imaging and Surgical Innovation, Richardson, Texas, United States

³University of Texas Southwestern Medical Center, Department of Radiology, Dallas, Texas, United States

ABSTRACT. **Significance:** Early detection of Alzheimer's diseases, diabetic retinopathy, or macular degeneration with advanced retinal imaging technologies can help improve patient care and treatment outcome.

Aim: We aim to create a high-resolution hyperspectral imaging (HSI) system for the retina. Retinal vessel diameter and oxygenation rate will be extracted simultaneously from HSI data.

Approach: Our hyperspectral retinal imaging system consists of a snapshot hyperspectral camera, a high-resolution RGB camera, a beamsplitter, and an imaging endoscope. Multiple pansharpening algorithms, including deep learning methods, were developed to generate high-resolution hyperspectral images that were further used for the measurement of vessel size and oxygenation rate in mice.

Results: The hyperspectral retinal imaging system was tested for its spatial resolution and spectral fidelity in retina phantoms. *In vivo* imaging experiments were performed in mice. The deep learning-based pansharpening algorithm achieved a root mean square error (RMSE) of 2.15 ± 0.64 , a correlation coefficient (CC) of 0.96 ± 0.05 , a spectral angle score of 0.06 ± 0.03 radians, and an error relative global dimensionless synthesis (ERGAS) score of 2.37 ± 1.71 . Oxygen saturation (sO_2) and lumen diameters of blood vessels were measured in the retina. The average lumen diameter of the venules was $45.7 \pm 13.6 \mu\text{m}$, whereas the average lumen diameter of the arterioles was $31.5 \pm 8.7 \mu\text{m}$. The average arteriole sO_2 was 98%, whereas the average venule sO_2 was 58%.

Conclusions: A high-resolution hyperspectral imaging system was developed and validated for retina imaging and measurement of blood vessels and oxygen saturation.

© The Authors. Published by SPIE under a Creative Commons Attribution 4.0 International License. Distribution or reproduction of this work in whole or in part requires full attribution of the original publication, including its DOI. [DOI: [10.1117/1.JBO.31.3.036006](https://doi.org/10.1117/1.JBO.31.3.036006)]

Keywords: retina; hyperspectral imaging; topical endoscopic fundus imaging; oxygen saturation

Paper 250346GR received Nov. 6, 2025; revised Feb. 2, 2026; accepted Feb. 24, 2026; published Mar. 18, 2026.

1 Introduction

Biological tissues hold essential spectral information that reflects their physiological and pathological states.¹ Traditionally, spectrometers were used to analyze these spectral signatures, but their limited spatial coverage restricted their utility. Hyperspectral imaging (HSI) has emerged as a transformative technology to overcome this limitation, offering a three-dimensional data cube,

*Address all correspondence to Baowei Fei, bfei@utdallas.edu

or hypercube, that integrates both spatial and spectral information. By capturing an extensive range of spectral signatures across large spatial areas, HSI has proven to be superior to traditional RGB imaging in various biomedical applications, such as quantifying blood oxygenation.² Recent advancements in manufacturing and optical technologies have significantly improved the accessibility of HSI systems, making cameras more compact, portable, and affordable, further fueling interest in biomedical diagnostics.³

The retina, an extension of the central nervous system (CNS),⁴ provides crucial insights into CNS-related conditions such as multiple sclerosis, Alzheimer's disease (AD), and stroke. Conventional retinal imaging techniques, including fundus imaging, retinal angiography, and optical coherence tomography (OCT), are widely employed to investigate retinal biomarkers such as oxygen saturation and retinal layer thickness. However, these methods have inherent limitations. Angiography is invasive, whereas fundus imaging and OCT, although noninvasive, are incapable of measuring blood vessel oxygenation. By contrast, HSI offers a compelling alternative by detecting specific spectral signatures associated with retinal biomarkers. Specifically, several retinal biomarkers can be detected using HSI. Oxygenation rate, or sO_2 for short, measures the percentage of oxygen bound to hemoglobin as a percentage of maximum possible oxygen bound. Because oxyhemoglobin and deoxyhemoglobin have different absorption coefficients,¹ HSI can estimate the ratio of bound hemoglobin to unbound ones. The diameter of the arterioles and venules can serve as predictors of retinal physiology.^{5,6} They can be measured if the magnification factor of the HSI system is known. Using either of these biomarkers in the retina, HSI has demonstrated its effectiveness in monitoring diabetic retinopathy, radiation retinopathy, age-related macular degeneration (AMD), and Alzheimer's disease (AD).⁵⁻⁹

Despite these advances, retinal imaging using HSI presents various technical challenges. For instance, protecting the retina from excessive exposure requires minimizing imaging duration and ensuring that illumination levels remain within safe limits.³ These constraints influence the choice of spectral acquisition hardware. Push-broom and spectral-scanning cameras, while capable of high spectral resolution, often take several seconds or up to minutes to complete a single scan, making them impractical for retinal imaging. Snapshot hyperspectral imaging systems, particularly those leveraging spectrally resolved detector arrays (SRDAs), offer a viable alternative by capturing hyperspectral data in real-time. SRDAs utilize CMOS sensors with mosaic-patterned filters to create hypercubes through processing. Recent engineering innovations have made SRDA systems increasingly attractive for retinal imaging due to their compact form factor (weigh less than 100 grams) and their fast acquisition time (orders of milliseconds per hypercube).³ However, SRDA-based snapshot systems face trade-offs, most notably in spatial resolution. The lower raster size of their images can obscure critical microvascular details necessary for accurate diagnosis.

To address these limitations, pansharpening techniques, which were commonly used in remote sensing, have been employed to combine low-resolution hyperspectral images with high-resolution monochromatic images to create high-resolution hyperspectral data. Although pansharpening has been extensively applied in remote sensing,¹⁰⁻¹² its use in biological imaging remains limited, with only a few notable examples, such as the work by Ma et al.¹³ Building on this idea, we propose a novel dual-camera system that integrates snapshot hyperspectral imaging with high-resolution RGB imaging. Our approach is an extension of the topical endoscopy fundus imaging (TEFI) system, which is a cost-effective method to image retina of small mammals.¹⁴ To enhance this system, we developed a software workflow capable of merging hyperspectral and RGB images, resulting in high-resolution hyperspectral images. Unlike previous TEFI-based method that used a beamsplitter for simultaneous fluorescence and RGB imaging,¹⁵ our system is the first to incorporate hyperspectral pansharpening in a beamsplitter configuration within TEFI.

Our contributions are: (1) The development of a high-speed, high-resolution hyperspectral imaging system capable of robust imaging in an animal model. (2) An in-depth investigation of pansharpening methods applied to hyperspectral images of biological tissues. (3) A validation study using retinal phantoms and *in vivo* mouse imaging, wherein we extracted retinal vessel diameters and measured blood vessel oxygenation rates. This dual-camera system, combined with advanced pansharpening techniques, offers a promising solution for high-resolution hyperspectral retinal imaging, opening new avenues for both diagnostic and research applications.

2 Methods

2.1 Hardware Overview

2.1.1 System construction

Figure 1 shows the standard configuration of our system. The system consisted of a snapshot hyperspectral imaging camera, a high-resolution RGB imaging camera (ToupTek C3CMOS series, ToupTek Photonics, China), an optical beamsplitter (BS019, Thorlabs, Newton, New Jersey, United States), an imaging endoscope (1218AA, Karl Storz, Germany), and fixed focal length (FFL) imaging lenses. The HSI snapshot camera (MQ022HG-IM-SM4X4-VIS3, Imec, Belgium) captured 16 bands of images at an image resolution of 270×510 pixels from 460 to 600 nm through bandpass filters arranged in an alternating pattern.¹⁶ The RGB camera is a standard scientific CMOS camera with an image resolution of up to 2048×3072 pixels. We designed the system for the imaging of mouse retinas. However, the system is easily adaptable for the human retina by simply using an endoscope with a larger diameter. The diameter of the scope's illuminating crescent should be similar to that of a fully dilated mouse pupil (around 3 mm).¹⁷ We chose an otoscope with a diameter of 3 mm and a length of 6 cm for this purpose. Illumination was provided from a xenon illumination source (CLV-S200-IR, Olympus, Tokyo, Japan) through a fiber guide. Finally, a series of fixed focal length lenses was needed to provide magnification. Table 1 shows the configurations of our system. The system was placed on a translation platform (PT1, Thorlabs, Newton, New Jersey, United States), which in turn was placed on top of a rotational platform (SL20, Thorlabs, Newton, New Jersey, United States). This gives our system four degrees of freedom (three rotations plus forward/backward translation) so that it can be used for a variety of targets.

2.1.2 Optical capability

We identified the closest focusing distance using a United States Air Force (USAF) 1951 resolution chart (Thorlabs, Newton, New Jersey, United States), with 54 markings divided into eight groups of different resolutions. The resolution is determined by the smallest pairs of markings

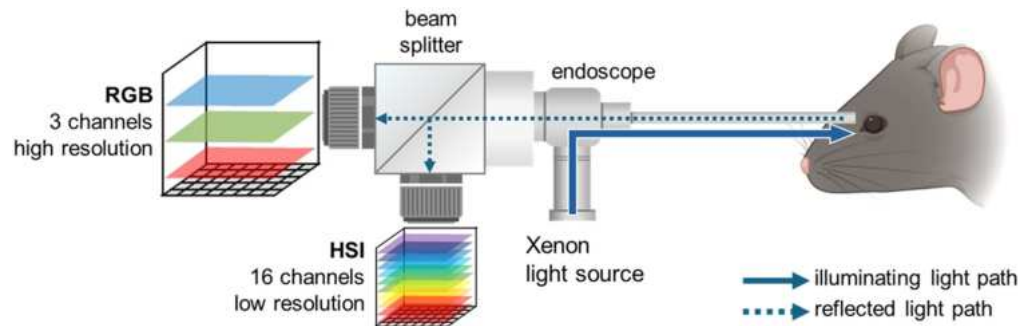


Fig. 1 Diagram of the system used to produce both high-resolution RGB and hyperspectral images simultaneously.

Table 1 Configurations of our systems.

RGB camera	2048 × 3072-pixel imaging camera
HSI camera	270 × 512 pixel × 16 channels HSI camera
Beamsplitter	70% transmitting, 30% reflecting non-polarizing optical beamsplitter
Imaging scope	3 mm diameter borescope
RGB imaging lens	35 mm FFL lens
HSI imaging lens	25 mm FFL lens

that can be resolved. A line is drawn through each pair of markings, and then a sine curve with values ranging from S_{\min} to S_{\max} is fitted to the intensity value. The contrast between the lines and the spaces was calculated using the formula $\text{contrast} = (S_{\max} - S_{\min}) / (S_{\max} + S_{\min})$.¹⁸ With the FFL lens at the nearest possible focus, we placed the target touching the tip of the scope. Then, we slowly moved the target away until it was in focus. The distance translated was the nearest focus of the system. The system is viable for mouse retinal imaging if the object distance is farther than the nearest focus distance. We identified barrel distortion using the system to image a square checkerboard grid. Distortion was automatically corrected using a customized MATLAB program, and the correction amount was used for subsequent images.

Spectral performance of the snapshot camera was measured using color diffuse reflectance standards made out of Spectralon (Labsphere, North Sutton, New Hampshire, United States). There are eight tiles in total (blue, cyan, green, orange, purple, red, violet, and yellow). The tiles were placed 5 mm from the distal end of the scope. For comparison, we independently measured the reflectance using a spectrometer (Ocean Insight, Orlando, Florida, United States). The setup used for measuring the spectral performance was similar to that used by Pruitt et al.¹⁹ The reflectance standards were placed at a distance 6 mm away from the tip of the endoscope, at the location where the mouse would be situated. Illumination was provided by Xenon light through a fiber optic light guide. The spectrometer used a fiber probe, which we pointed toward the reflectance standard tiles. The values measured using snapshot camera and spectrometer were compared against the calibrated value, which was measured by the manufacturer using a spectrophotometer. We interpolated the reflectance measurements of the spectrometer and the factory calibration data to the wavelengths of the HSI camera. The method used to calculate errors was root mean square error (RMSE), which was defined as

$$\text{RMSE} = \sqrt{\frac{\sum_{i=1}^N (x_i - \hat{x}_i)^2}{N}}, \quad (1)$$

where \hat{x}_i and x_i are the factory calibrated and the measured intensity values of the spectral bands, respectively, and N is the number of spectral bands sampled by the spectrometer or the HSI camera.

2.2 Acquisition Steps

Animal experiments were conducted under Protocol 2023-0098, approved by the University of Texas at Dallas Institutional Animal Care and Use Committee (IACUC). Using the system described, we acquired hyperspectral images of the retina in C57BL/6 black mice and wild-type mice (Jackson National Labs, United States). Our procedure was based on the procedure described by More et al.²⁰ Fifteen minutes prior to the anesthesia, we applied 2.5% phenylephrine hydrochlorine and 0.5% tropicamide onto each eye for pupil dilation. Mice were anesthetized by inhalation of 5% isoflurane mixed with medical air until immobile, then remained anesthetized by inhalation of 2% isoflurane. Mice were placed in a customized imaging platform [Figs. 2(a) and 2(b)] that allowed restraints and rotations of the animal. We applied local anesthetic (Proparacaine, Fisher Scientific, United States), followed by a gel eye drop (Gentel Tears, Alcon, United States) to the cornea. We placed mice on top of the vertical translation platform, then rotated the imaging platform toward the surface of the cornea [Fig. 2(c)]. Then, we translated the entire imaging system forward until the scope contacted the cornea at a direct angle [Fig. 2(d)]. We then changed the focus on the FFL lens until the retina was in focus. The exposure time for the RGB camera was 100 ms, whereas the exposure time for the HSI camera was 200 ms. The entirety of imaging lasted less than 5 min per mouse, which was enough for the anesthetized mouse to return to its cage and recover.

2.3 Generating High-Resolution Hyperspectral Images

To produce high-resolution images, we created an automatic imaging workflow. The workflow has three stages: pre-processing, registration, and pan sharpening. For preprocessing, the same pipelines were used for RGB images and hyperspectral images. The images were corrected with white and dark references using the following equation:

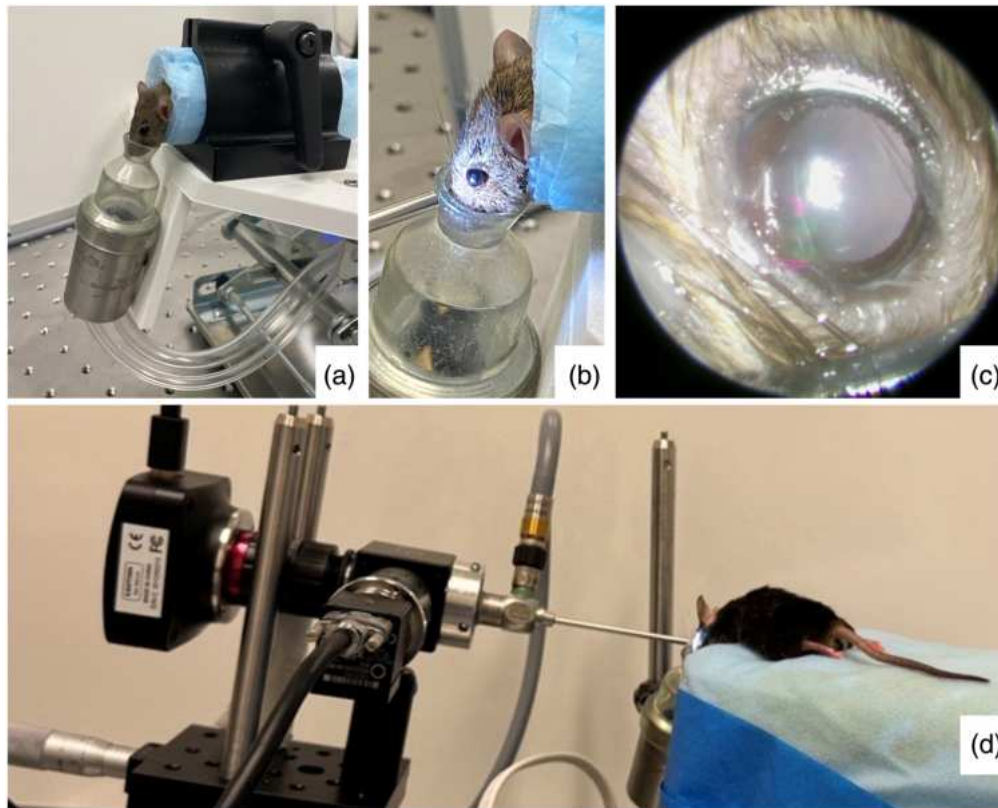


Fig. 2 Acquisition of mice retinal images. (a) Mouse placed under anesthesia in our customized platform. (b) Mouse eyes were dilated with phenylephrine and tropicamide. (c) Fully dilated eye, from the viewpoint of the endoscope. (d) System acquisition of mouse eye.

$$I = \frac{I_{\text{raw}} - I_{\text{dark}}}{I_{\text{white}} - I_{\text{dark}}}, \quad (2)$$

where I_{raw} is the raw acquired image, I_{dark} is the dark reference image, I_{white} is the white reference image, and I is the final corrected image. This method also achieves white-balance correction in the RGB image. To get the white reference image, we used the cameras to image a Spectralon tile placed 4 mm away from the endoscope tip, which was the object distance of the mouse retina.

We registered the high-resolution RGB images to low-resolution hyperspectral images under the conditions that only translation, scaling, and rotation are involved. Registration was performed manually and done in Photoshop software. For clarity, we used the term “hyperspectral images” to refer to the original image of $510 \times 270 \times 16$ pixels and used the term “pansharpened images” to refer to the $3072 \times 2048 \times 16$ images that are the product of combining the RGB image and the HSI.

2.3.1 Methods

We tested several different methods for image pansharpening and compared multiple published methods in our application. A list of the tested methods is shown in Table 2. In general, pansharpening assumes that a higher-spatial-resolution image (here, the registered RGB image) contains spatial detail that can be transferred to a lower-spatial-resolution spectral data product (here, the HSI cube) without substantially altering its spectral signatures. After registration, the RGB image is used to estimate high-frequency spatial structure, such as edges and fine textures, which is then injected into each hyperspectral band through a fusion rule that either modulates the band intensities or adds a high-pass detail component. The resulting product preserves the band-wise spectral information from the HSI while adopting the spatial detail implied by the higher-resolution RGB image, yielding a hyperspectral cube at improved spatial resolution. The choices of methods were taken from a review paper by Javan et al.²⁴ Bicubic interpolation (BCB) resamples the image using cubic convolution. The Brovey algorithm (BV) combines spectral and

Table 2 Overview of methods tested in the paper to produce pansharpened images.

Method	Abbreviation
Classical Methods	
Bicubic interpolation	BCB*
Brovey algorithm ²¹	BV*
Generalized intensity–hue–saturation ²¹	GIHS*
Adaptive Gram-Schmidt	GSA*
Gram-Schmidt	GS*
High-pass filtering using 13×13 box filter	HPF*
Undecimated “à trous” wavelet substitution ²²	UDWT*
Deep Learning Methods	
Convolutional neural network ¹¹	CNN
Generative adversarial network ²³	PSGAN
Unsupervised generative adversarial network ¹²	PAN-GAN*
U-Net ¹³	UN*

The star * indicates that the method is unsupervised.

panchromatic images by normalizing and scaling each band.²¹ Gram-Schmidt (GS) uses orthogonalization to merge the images.²⁴ Adaptive Gram-Schmidt (GSA) uses least-squares minimization to generate images prior to merging using GS.²⁴ Generalized intensity-hue-saturation (GIHS) method transforms the spectral image into intensity, hue, and saturation components, replaces intensity with the panchromatic image, and converts it back.²¹ High-pass filtering (HPF) adds spatial details from the panchromatic image.²⁴ Undecimated discrete wavelet transform (UDWT) injects details using wavelet decomposition.²² In addition, we tested several deep learning-based architectures, including a convolutional neural network architecture from Masi et al.,¹¹ supervised generative adversarial network (GAN) from Liu et al.²³ and Ma et al.,¹² and unsupervised U-Net from Ma et al.¹³

Our experiments found that PSGAN is the best-performing method for pansharpening. Hence, it is of the reader’s interest that we describe its working further. PSGAN consists of two networks: a generator and a discriminator. The architecture of the generator is that of a U-Net. The U-Net architecture in this generator is three layers deep and two layers wide. After registration, the RGB image is perturbed by a small random adjustment in hue, saturation, and value to preserve the underlying spatial structure while introducing slight spectral variation. The output of the generator is a high-resolution HSI (HSI_{HR}), with the same height and width as that of the RGB image and the same number of channels as that of the HSI. The high-resolution HSI is down-sampled by a factor of 4 using a bi-linear sampling algorithm. The output will be a low-resolution HSI (HSI_{LR}), with the same dimension (height, width, and number of channels) as that of the original HSI input. A spectral loss function compares the low-resolution HSI with the input HSI for spectral loss $\mathcal{L}_{\text{spectral}} = \text{RMSE}(HSI_{LR} - HSI_{\text{input}})$. Similarly, a perceptual loss (spatial loss) function is derived from a pretrained VGG network, which compares the activation output at different layers:

$$\mathcal{L}_{\text{spatial}} = \sum_l \frac{1}{C_l H_l W_l} \|\phi_l(HSI_{LR}) - \phi_l(HSI_{\text{input}})\|_2^2. \quad (3)$$

Here, ϕ_l is the feature map extracted from the layer l of a pre-trained VGG network, C_l, H_l, W_l are respectively the number of channels, height, and width of the feature map at layer l of the pretrained network. $\|x\|_2^2$ is the squared Euclidean norm of the vector x .

The generator's objective is to minimize the combined loss function while simultaneously fooling the discriminators into classifying the generated images as high-quality outputs. Conversely, the discriminator aims to maximize its ability to distinguish real data from generated outputs, thereby creating a competitive dynamic that enhances the generator's performance over successive iterations. For the spectral discriminator, the adversarial loss is given by

$$\begin{aligned}\mathcal{L}_{\text{adv_spectral}} = & -\text{E}[\log(D_{\text{spectral}}(\text{HSI}_{\text{real}}))] \\ & - \text{E}[\log(1 - D_{\text{spectral}}(\text{HSI}_{\text{generated}}))].\end{aligned}\quad (4)$$

Similarly, for the spatial discriminator, the adversarial loss is

$$\begin{aligned}\mathcal{L}_{\text{adv_spatial}} = & -\text{E}[\log(D_{\text{spatial}}(\text{HSI}_{\text{real}}))] \\ & - \text{E}[\log(1 - D_{\text{spatial}}(\text{HSI}_{\text{generated}}))].\end{aligned}\quad (5)$$

Here, E refers to the expected value (averaged log values), whereas D refers to the output of the discriminator. The generator minimizes a weighted combination of the spectral loss and spatial loss to balance spatial and spectral accuracy. The combined loss function is expressed as

$$\mathcal{L} = \alpha(\mathcal{L}_{\text{spectral}} + \mu\mathcal{L}_{\text{spatial}}) + \beta(\mathcal{L}_{\text{adv_spectral}} + \gamma\mathcal{L}_{\text{adv_spatial}}),\quad (6)$$

where α and β are respectively the weighing factors for the generator loss and the discriminator loss, whereas μ and γ are the weighing factors for the generator spatial loss and the adversarial spatial loss, respectively. The generator was first trained by setting $\alpha = 1$ and $\beta = 0$. Then, we trained the discriminator using $\alpha = 10^{-3}$, $\beta = 0.06$, $\mu = 0.2$, and $\beta = 1$.

2.3.2 Model training

The same training protocol was performed on all four deep learning-based pansharpening methods. Model training was performed using the Harvard dataset.²⁵ The Harvard Real-World Hyperspectral Images Database is a publicly available benchmark of real indoor and outdoor scenes captured under controlled illumination, with each image providing 31 spectral bands across the visible range (~420 to 720 nm). It is commonly used to train and evaluate methods that learn mappings between low- and high-resolution spectral content because it supplies dense, band-aligned spectra at each pixel. The dataset consists of 50 real-life images of dimension $1392 \times 1040 \times 31$ (h \times w \times c). During the training, we randomly cropped each image to a size of 256×256 pixels. The low-resolution image was generated by downsampling the high-resolution HSI to a size of 64×64 pixels, then adding random Gaussian noise. The goal of training was to produce high-resolution HSI patches of size $256 \times 256 \times 16$ pixels. Evaluation was performed on the CAVE dataset.²⁶ The CAVE Multispectral Image is another standard benchmark consisting of laboratory-captured scenes provided as reflectance data sampled from 400 to 700 nm in 10 nm steps (31 bands), typically at 512×512 spatial resolutions. For this dataset, we center-cropped every image to a size of 256×256 pixels. Training was performed on a high-performance GPU cluster consisting of 8 NVIDIA 64Gb GPUs. Trainings for deep learning methods were performed using Adam optimizer with a learning rate of 1×10^{-4} , mean squared error (MSE) loss, and a batch size of 16.

2.3.3 Evaluation

We employed several metrics to evaluate pansharpening techniques. The goal is to ensure that the pansharpened, high-resolution image preserves both the spectral fidelity (compared to the hyperspectral image captured by the snapshot camera) and the spatial fidelity (compared to the RGB image captured by the CMOS camera). The final pansharpened images were compared to the ground truth in our training dataset. We used spectral angle mapper (SAM), RMSE, error relative global dimensionless synthesis index (ERGAS), and two-dimensional correlation coefficient (CC) to compare the spatial and spectral distortion.¹⁰ Let H be the ground truth hyperspectral image (the original hyperspectral image), and let P be the result of the pansharpening algorithm. Let x , y , and z be the coordinates of the pixels in the images, with z being the spectral dimension. SAM compares the angle between the corresponding pixels i in the fused image and the original image using the following equation:

$$\text{SAM} = \frac{1}{N_x} \frac{1}{N_y} \sum_{x=1}^{N_x} \sum_{y=1}^{N_y} \arccos \left(\frac{\langle H_{(x,y)}, P_{(x,y)} \rangle}{\|H_{(x,y)}\| \|P_{(x,y)}\|} \right) \quad (7)$$

The SAM metric is obtained by averaging the angle measurements across all pixels. A smaller SAM value represents better spectral similarity, with a minimum value of 0.

ERGAS is a refinement of RMSE by accounting for errors across different bands. ERGAS is defined as follows:

$$\text{ERGAS} = \frac{100}{4} \sqrt{\frac{1}{C} \sum_{z=1}^C \left(\frac{\text{RMSE}(H_z, P_z)}{\mu(H_z)} \right)^2}. \quad (8)$$

The ratio 100/4 came from the ratio between the size of the small hyperspectral image and the large RGB image. C is the number of channels, and $H[j]$ indicates the j^{th} spectral channel. Smaller ERGAS is better, with a minimum value of 0.

Two-dimensional correlation coefficient (CC) score measures how well two images agree with each other. It is defined as

$$\text{CC} = \frac{\sum_{x,y} ((H_{(x,y)} - \mu_H) \odot (P_{(x,y)} - \mu_P))}{\sqrt{\sum_{x,y} (H_{(x,y)} - \mu_H)^2 \sum_{x,y} (P_{(x,y)} - \mu_P)^2}}. \quad (9)$$

Here, μ_H and μ_P indicates the mean of H and P , respectively. The symbol \odot indicates an element-wise product (Hadamard product). CC score ranges from 0 to 1, with higher CC score being better.

2.4 Measuring Vessels' Diameters

2.4.1 Algorithms

We converted measurements made in retinal images to physical size, *i.e.*, converting pixel values to microns. We did not attempt to perform any theoretical evaluations to estimate the retinal magnification factor of the mouse eye. Instead, we proposed an engineering-based approach to calculate the magnification factor. First, we imaged the mouse retinas under anesthesia. With the tip of the endoscope touching the cornea, we adjusted the FFL lens so that the retina was in focus. The distance between the tip of the endoscope and the back of the retina is the object distance (d_o for short). This distance is not exactly known; we assumed d_o to be the diameter of the eyeball. Keeping the same focus on the FFL lens, we placed the USAF target at the tip of the endoscope. Then, we slowly moved the USAF target away from the lens until the markings were in focus. The distance between the tip of the endoscope and the USAF target is the image distance (d_i for short). With the assumption that the eye contains a single crystalline lens, we can find the magnification factor of the mouse eye:

$$M_{\text{eye}} = \frac{d_i}{d_o}. \quad (10)$$

To find the pixel-to-micron ratio of the optical system, we placed a microscope graticule (a glass piece with a measurement scale on its surface) at the same distance away from the endoscope tip as the image distance. The micron-to-pixel conversion factor of the endoscope is

$$m_{\text{system}} = \frac{1000}{\text{Number of pixels to cover 1 mm}}. \quad (11)$$

The total magnification of the system when imaging mouse eyes is the product of the lens magnification factor and the endoscope system magnification factor. Its unit is micron/pixel:

$$m_{\text{conversion}} = m_{\text{system}} \times M_{\text{eye}}. \quad (12)$$

We used ImageJ software²⁷ to measure the diameter of the vessels in pixels. The diameter of the vessels was converted to physical values using the following equation:

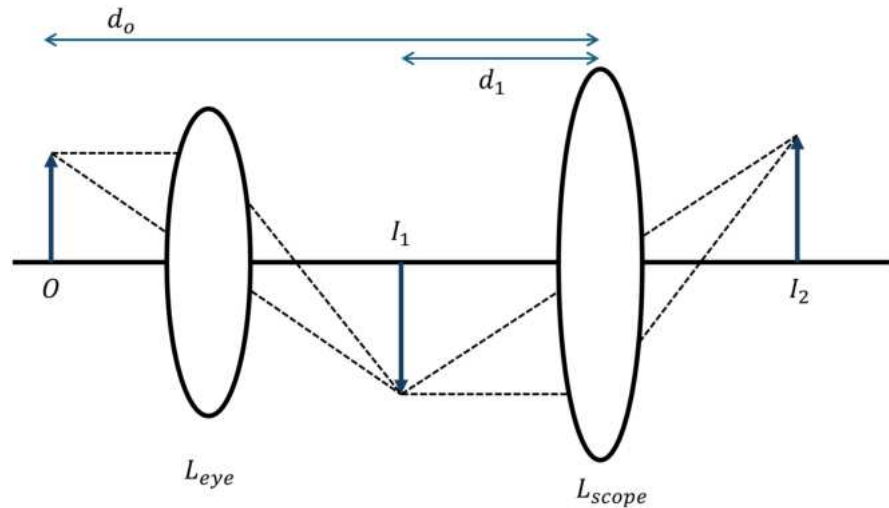


Fig. 3 Simple ray diagram that illustrates the reasoning behind our magnification equation.

$$\text{Size in } \mu\text{m} = \text{Size in pixel} \times m_{\text{conversion}} \quad (13)$$

Figure 3 illustrates the principles behind our magnification equation. The object located at O is the back of the retina, which we wanted to image. The eye lens L_{eye} produces an image located at I_1 . The scope and the FFL L_{scope} produces an image located at I_2 that is measured by the sensor. Assuming that the scope and the lens are in close contact with each other, d_o approximate the distance between the object and the scope, and d_1 approximates the distance between Image I_1 and the scope.

2.4.2 Validation

We validated diameter extraction on a series of mouse retinal phantoms. Mouse retina phantom was 3D printed by modifying a design by Hosseinaee et al.²⁸ Figures 4(a) and 4(b) shows the 3D model of the mouse eye phantom. The lens holder was created to model the lens size, axial length, and focal length of a mouse eye. Our lens holder accommodates a model mouse lens (4 mm lens, Uxcell, Hong Kong, China) with a diameter of 4 mm (~ 0.16 in) and a height of 2.3 mm (~ 0.09 in), effectively simulating the natural curvature of a mouse lens. One key aspect considered during the design process was the smaller vitreous-to-lens ratio in mouse eyes compared with human eyes. In mice, the lens occupies nearly 75% of the eye. To replicate this proportion, the anterior chamber phantom features a spherical interior with a diameter of 3.10 mm (~ 0.10 in) and a depth (focal length) of 3 mm (~ 0.12 in) from the lens. The design process was carried out using Creo Parametric computer-aided design (CAD) software. The final design uses generic PLA white filament as its material, which has an average assumed rate of shrinkage range of 0.8% to 3%. The model was 3D printed using a Bambu Lab X1 Carbon 3D printer with a 0.4 mm (about 0.02 in) nozzle head. The interior of the retina phantom was filled with carbon fiber strands [Fig. 4(c)]. Using the algorithms described earlier, we identified the focus of the FFL lens such that carbon fiber strands in the optical model were clearly seen. Then, we removed the lens from the optical model and measured the lengths of the fiber strands using an upright microscope. The lengths of the carbon fiber strands calculated using the magnification formula were compared with the lengths of the strands measured using the microscope.

2.5 Measuring Vessels' Oxygenation

2.5.1 Algorithms

The spectra of the blood vessel are dependent on the surrounding background (the retina); hence, we need to subtract the influence of the retina from the vessel. To accomplish this, every pixel within the blood vessel is divided by the average spectrum of the surrounding retinal background in an 11×11 -pixel window. Then, the blood vessel reflectance spectrum R was converted to optical density OD using the formula $OD = -\log_{10} R$. Then, the optical densities were

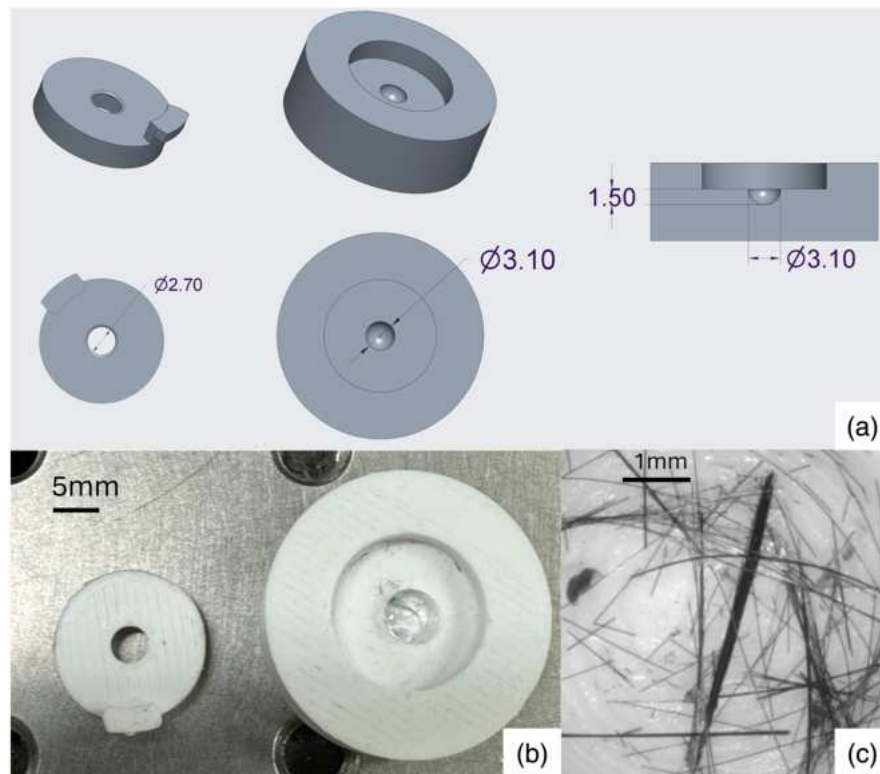


Fig. 4 Design of the mice retinal phantom. The dimensions are stated in mm. Panel (a) shows the designs and dimensions of the iris phantom. Panel (b) shows the printed system with the lens in place. Panel (c) shows the interior chamber filled with carbon fiber strands.

normalized using spectral normal variance (SNV) normalization. SNV subtracts the optical density (OD) by its mean μ_{OD} , then divides by its standard deviation σ_X using the formula $SNV = (OD - \mu_{OD})/\sigma_{OD}$. Then, we used multiwavelength curve fitting to estimate the oxygen saturation values.²⁹ For each pixel within the blood vessel, we found the solution of the following equation:

$$OD(\lambda) = B - N \ln(\lambda) + A[\mu_{\text{HbO}_2}(\lambda) + (1 - s\text{O}_2)\mu_{\text{Hb}}] \quad (14)$$

Here, B and N are the constant terms that model the linear and non-linear scattering contributions, respectively. A is the thickness of the blood vessel (which scales the absorbance according to the Beer–Lambert law). $s\text{O}_2$ is the oxygen saturation that we wanted to find. The values of $\mu_{\text{Hb}}(\lambda)$ and $\mu_{\text{HbO}_2}(\lambda)$ are the wavelength-dependent absorption coefficients of deoxygenated and oxygenated hemoglobin, respectively. To find the endmembers values of $\mu_{\text{Hb}}(\lambda)$ and $\mu_{\text{HbO}_2}(\lambda)$, we acquired the spectra of fully oxygenated and fully deoxygenated blood with our system. Oxygenated sheep blood was diluted into PBS solution to enhance the spectral differences in the visible light range. By mixing sodium dithionite³⁰ into a well plate containing sheep blood, we were able to obtain fully deoxygenated sheep blood. The oxygen saturation of the blood samples was independently verified using a blood gas analyzer (Stat Profile Prime Plus, Nova Biomedical, Massachusetts, United States). Figure 5 shows the absorption spectra of oxygenated and deoxygenated blood, as captured by our hyperspectral camera. These spectra were different from the spectra obtained by Prah et al.³¹ due to the filter response in our camera.

2.5.2 Validation

To validate the oxygenation algorithm, we performed the following experiment with mice under anesthesia: mice were anesthetized using medical air (21% oxygen). After the first set of retinal images was captured, we replaced the medical air with pure oxygen (100% oxygen) and took a second set of retinal images. Previous studies showed that retinal oxygenation changed when

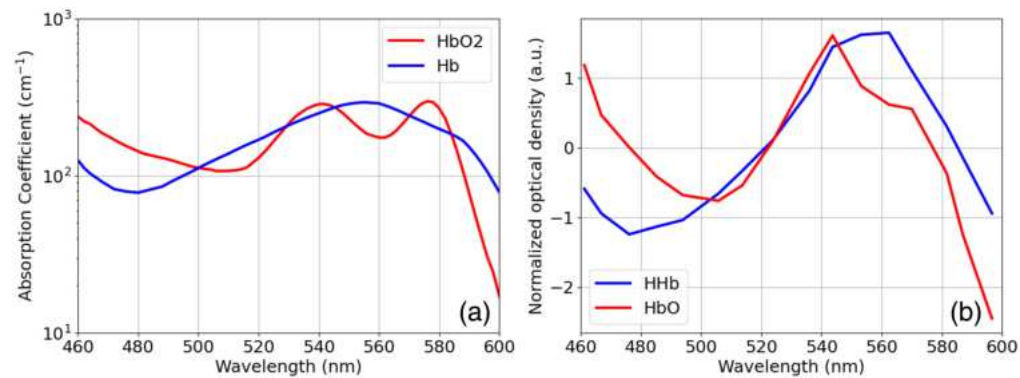


Fig. 5 Panel (a) shows the absorption coefficient of fully deoxygenated (blue) and fully oxygenated (red) blood, plotted from data by Prahl et al.³¹ Panel (b) shows the normalized optical density of fully deoxygenated (blue) and fully oxygenated (red) blood, taken by our hyperspectral imaging camera.

breathing pure oxygen.³² By comparing the oxygenation rate within the same vessel before and after breathing pure oxygen, we showed changes consistent with the literature.

3 Results

3.1 System Optical Performances

The nearest imaging distance of the system was 1.9 mm. Experiments showed that the imaging distance of the mouse retina ranges from 3.5 to 4 mm, which means that the system is fully capable of imaging mouse retina in focus. Figure 6 shows that the spatially resolvable resolution achieved by the system was 57 line-pairs/mm, or 17.5 microns. Figure 7 shows the respective diffuse reflectance curves from the HSI camera, spectrometer, and factory-calibrated values for each of the eight calibration tiles. Table 3 shows the RMSE of the HSI camera intensity and the spectrometer-measured value. The camera has an RMSE of $3.87 \pm 1.89 \times 10^{-2}$, and the spectrometer has an RMSE of $2.39 \pm 1.85 \times 10^{-2}$. The results showed that the HSI camera can achieve spectral accuracy comparable to that of a spectrometer.

3.3 Pansharpener Results

Table 4 shows the quantitative results of the different pansharpener algorithms. Figure 8 shows the results of applying pansharpener onto the retinal images. Figure 9 shows the results of applying pansharpener onto the USAF calibration target. We found that the hyperspectral image suffered from some motion blur. The results show that the Brovey method (BV), high-pass

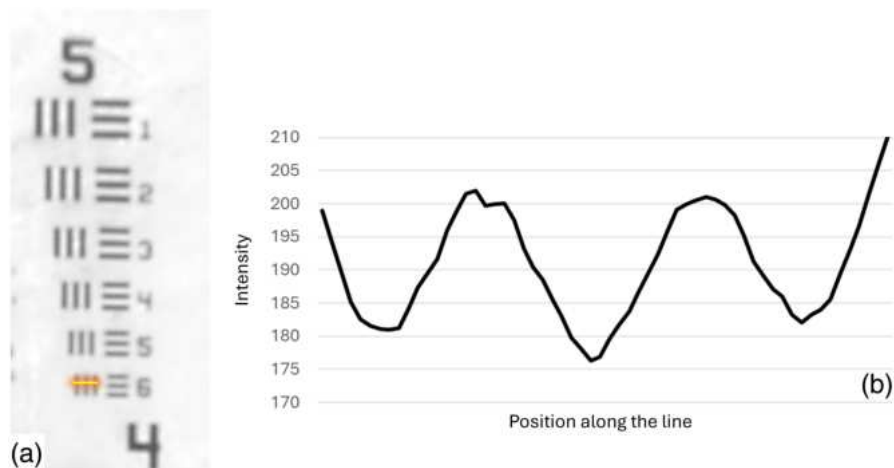


Fig. 6 (a) USAF target with resolvable resolution (contrast > 0.05) highlighted. (b) The intensity curve of the highlighted section.

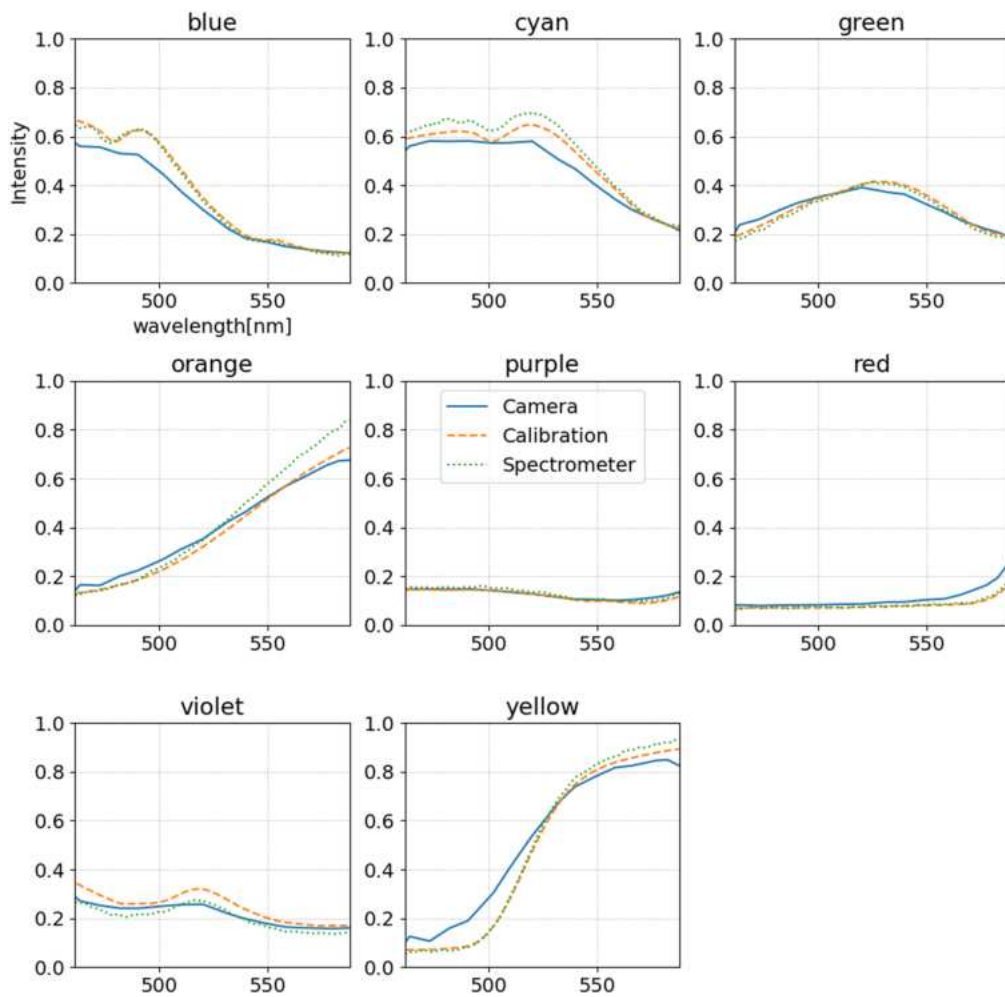


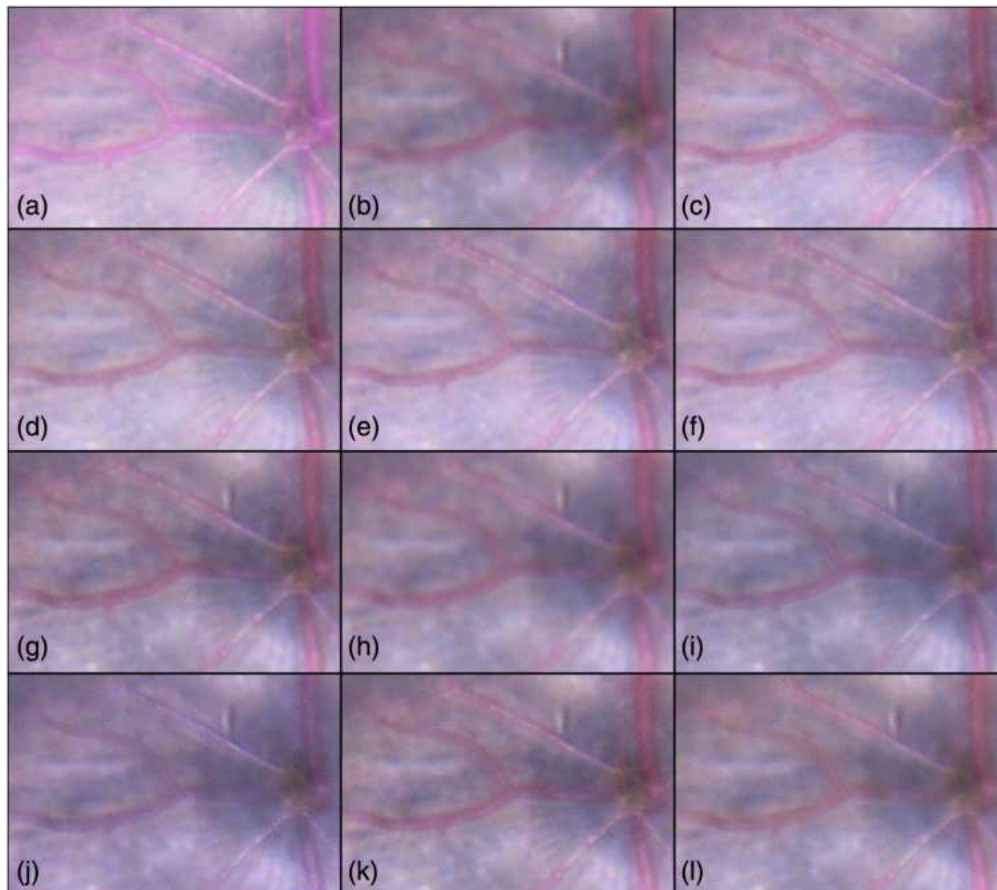
Fig. 7 Comparison between HSI camera intensity, spectrometer-recorded values, and factory-calibrated values.

Table 3 Comparison between reflectance values measured by HSI camera and spectrometer.

Tiles color	Camera RMSE ($\times 10^{-2}$)	Spectrometer RMSE ($\times 10^{-2}$)
Blue	6.15	1.13
Cyan	4.52	3.54
Green	2.39	1.15
Orange	3.01	5.36
Purple	0.95	0.89
Red	3.58	0.44
Violet	3.70	4.55
Yellow	6.65	2.09
Average \pm St. Dev.	3.87 ± 1.89	2.39 ± 1.85

Table 4 Quantitative result of pansharpening applied onto the test dataset. Bolded values mark the best performance on each metric.

Method	CC	RMSE ($\times 100$)	ERGAS	SAM
BCB	0.94 ± 0.08	4.64 ± 1.87	3.87 ± 2.38	0.04 ± 0.02
BV	0.94 ± 0.03	6.31 ± 2.76	6.15 ± 5.97	0.04 ± 0.02
GIHS	0.94 ± 0.03	6.11 ± 2.53	6.18 ± 6.27	0.11 ± 0.09
GS	0.94 ± 0.03	6.10 ± 2.53	6.09 ± 6.17	0.11 ± 0.09
GSA	0.94 ± 0.05	6.27 ± 2.74	6.65 ± 8.85	0.11 ± 0.09
HPF	0.96 ± 0.03	5.65 ± 1.66	4.80 ± 2.29	0.08 ± 0.04
UDWT	0.98 ± 0.01	2.74 ± 0.86	2.57 ± 1.93	0.05 ± 0.02
CNN	0.95 ± 0.05	2.33 ± 0.70	2.73 ± 2.45	0.07 ± 0.03
PSGAN	0.96 ± 0.05	2.15 ± 0.64	2.37 ± 1.71	0.06 ± 0.03
PAN-GAN	0.95 ± 0.05	4.01 ± 0.99	4.22 ± 2.96	0.10 ± 0.08
UN	0.88 ± 0.08	5.29 ± 1.34	6.78 ± 5.21	0.15 ± 0.07

**Fig. 8** Comparison of different pansharpening methods used to produce pansharpened image of the mouse retina. For purposes of visualization, the hyperspectral images were converted into pseudo-RGB using a method by Ma et al.³³ Because the conventional RGB image is captured by an RGB camera with an unknown response curve, we did not try to accurately recreate its color. The methods were described in Sec. 2. (a) Conventional RGB image. (b) Bicubic interpolation. (c) Brovey method, (d) IHS, (e) GS, (f) GSA, (g) HPF, (h) UDWT (i) CNN, (j) U-Net, (k) PSGAN, (l) PAN-GAN.

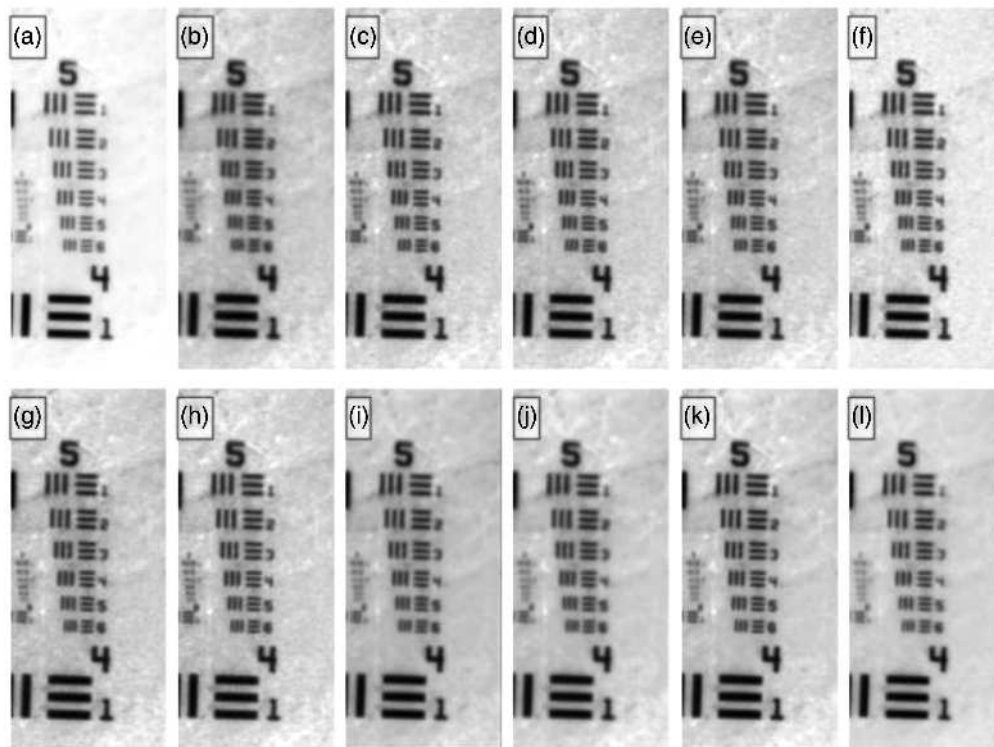


Fig. 9 Comparison of different pansharpening methods used to produce pansharpened images of the USAF targets. The methods were described in Sec. 2. (a) Conventional RGB image. (b) Bicubic interpolation. (c) Brovey method, (d) IHS, (e) GS, (f) GSA, (g) HPF, (h) UDWT, (i) CNN, (j) U-Net, (k) PSGAN, (l) PAN-GAN.

filtering (HPF), and methods based on neural networks best preserved the high-resolution structural details. PAN-GAN and U-Net models, owing to the fact that they were trained on unsupervised data, produced metrics that were slightly worse compared to other deep learning-based methods. We found that PSGAN produced the right balance between quantitative metrics and qualitative output. As such, for the analysis performed in the next sections, we use the pansharpened hyperspectral image produced by PSGAN. Figure 10 shows a selection of single-band images from the pansharpened hyperspectral image produced by PSGAN.

3.2 Measuring Vessels' Diameters

We measured the magnification factor of the phantom model mouse eye to be 1.2 \times , the optical magnification of the endoscope system at image distance to be 2.15 $\mu\text{m}/\text{pixel}$, and the conversion factor for retinal image to be 1.8 $\mu\text{m}/\text{pixel}$. Figure 11(b) shows a scatterplot of lengths estimated by our magnification factor algorithm and the actual measured value, showing an error rate of $7.6 \pm 5.6\%$. This shows that our conversion algorithm produces reasonable approximation of small details within the phantom retina.

We applied the vessels' diameter algorithm into live mice. Six eyes from three black-6 mice were used for our measurement. Within each mouse, 7-12 major vessels were found surrounding the optic nerve. The average lumen diameter of the venules was $45.7 \pm 13.6 \mu\text{m}$, whereas the average lumen diameter of the arterioles was $31.5 \pm 8.7 \mu\text{m}$. Literature shows that the diameter of retinal vessels in mice can range from 3.2 to 45.8 μm ,³⁴ which agrees with our measurements. There is a difference in the diameter of venules versus arteries. Because venules have more flexible lumens, they in general have larger lumen diameters.

3.4 Measuring Vessels' Oxygenation

Figure 12(a) shows the oxygenation map of the retina of a mouse breathing medical air (21% O_2). Figure 12(b) shows the oxygenation map of the retina of the same mouse breathing pure oxygen (100% O_2). Three vessels were found to have reduced oxygen saturation, likely because they

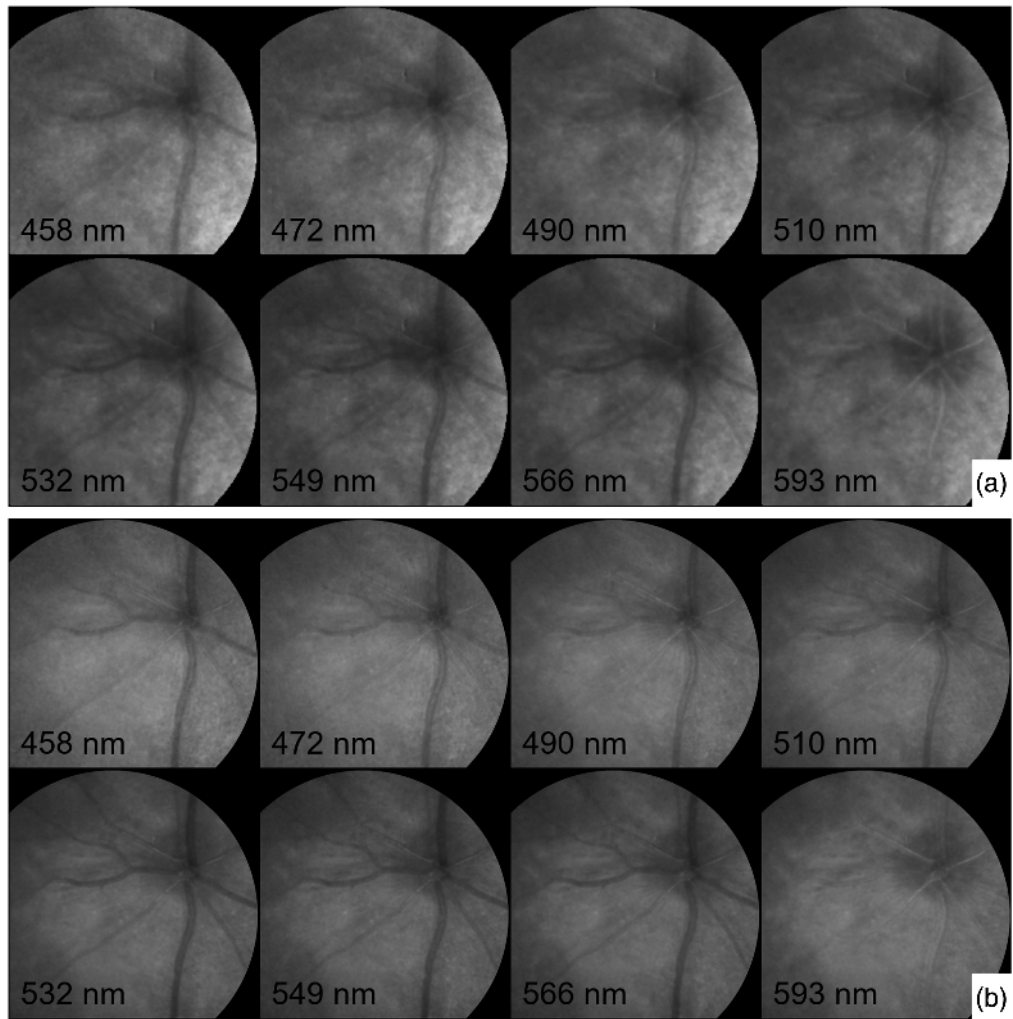


Fig. 10 (a) Original hyperspectral image of the retina. (b) Pansharpened hyperspectral image of the retina produced using the PSGAN method.

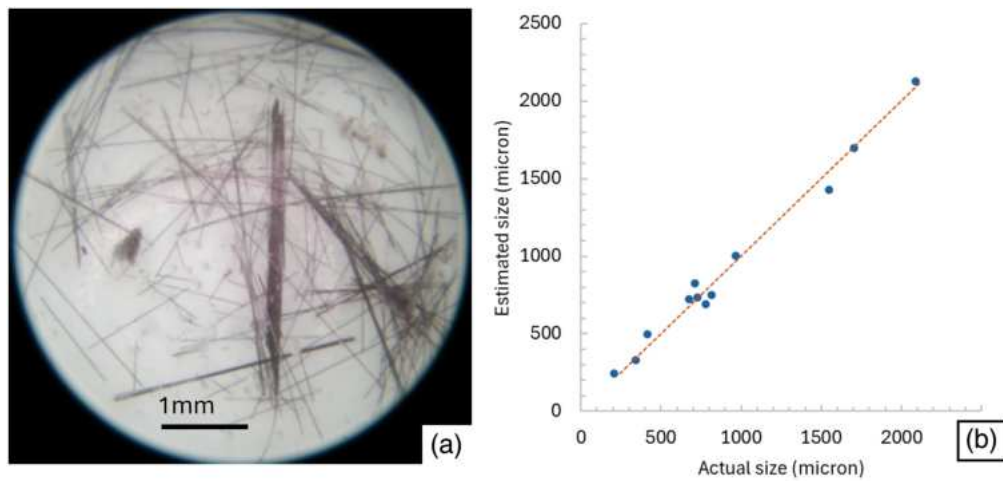


Fig. 11 (a) Retinal phantom image taken using our endoscopic system; (b) Differences between estimated and actual size of carbon fiber strands. Dashed lines indicate perfect linear correlation.

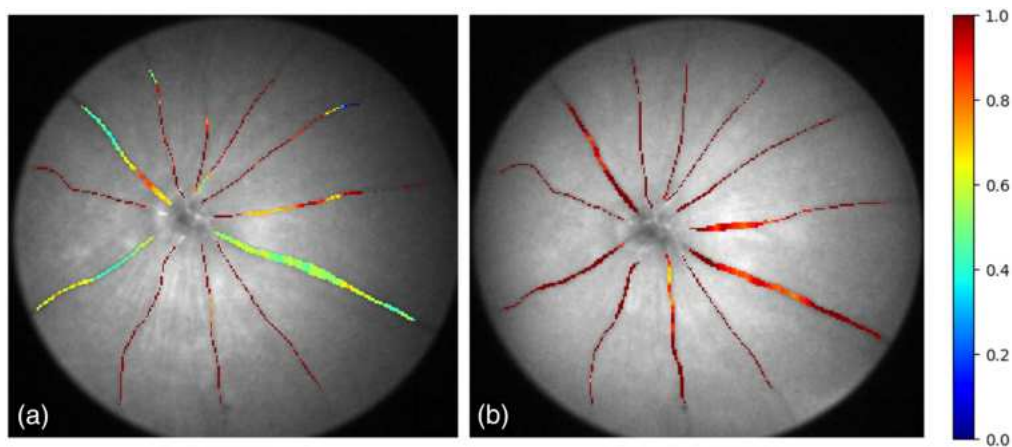


Fig. 12 (a) Oxygen saturation map of mouse breathing medical air. (b) Oxygen saturation map of the same mouse breathing pure oxygen.

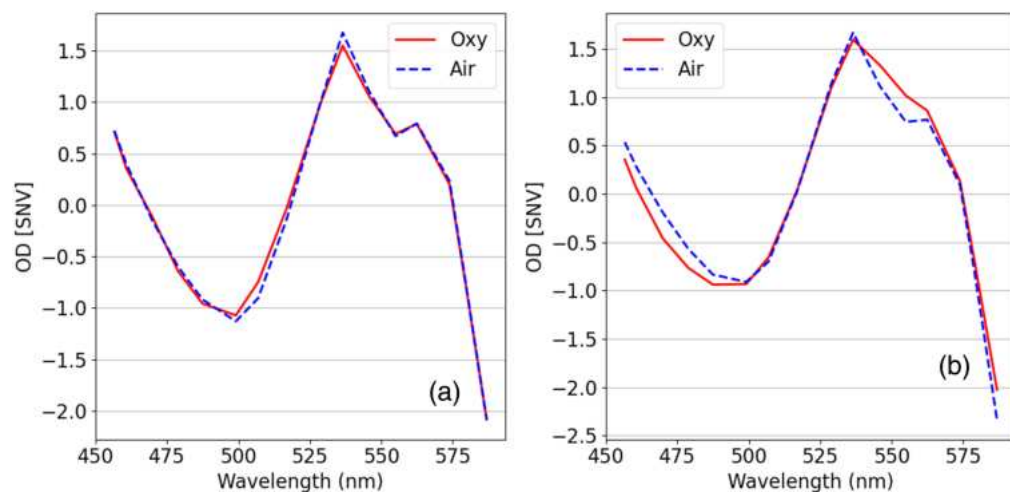


Fig. 13 Differences in the optical density of the same mouse, breathing medical air (orange) and breathing pure oxygen (blue). (a) Optical densities of arteriole showing no differences. (b) Optical densities of venule showing differences in the range 520-550 nm.

were venules. Examination of the optical densities of the vessels shows that there is a difference in the optical densities in the range 520 to 550 nm within the venules [Fig. 13(a)]. However, the arterioles show little difference in the optical densities [Fig. 13(b)]. We found consistent oxygen saturation within vessels, with the exception being along the edges of the vessels and close to the optic nerve. This is likely due to the fact that there is a significant presence of macular pigment near the optic nerve, making correct observation difficult. This problem has also been observed previously in the human retina.²⁹ The median arterioles sO_2 was 98%, whereas the median venules sO_2 was 58%.

4 Discussion and Conclusion

In this paper, we developed and validated a high-resolution hyperspectral imaging system and pansharpening methods for the retina. This approach allows for the simultaneous extraction of multiple retinal biomarkers, including oxygen saturation and the diameter of arterioles and venules. Although pansharpening is used in remote sensing, its application to *in vivo* hyperspectral imaging of tissues remains novel. Pansharpening methods were previously applied to histological and *ex vivo* tissue data.^{13,35,36} This work extended its use to *in vivo* imaging. The technique combines real-time hyperspectral acquisition capabilities of snapshot cameras with the high spatial

resolution of RGB cameras, potentially eliminating the trade-offs between speed, spatial resolution, and spectral detail that often limit hyperspectral imaging.

Through various trials and researching the literature, we developed a series of best practices to achieve optimal retinal imaging. First, the application of tropicamide or phenylephrine alone is not enough to achieve full eye dilation. Our experiences show that after repeated application of tropicamide, mice start to exhibit miosis (excessive constriction). A combination of 1% tropicamide and 1.5% phenylephrine achieved full dilation.³⁷ Eye drops should be applied prior to anesthesia or during a narrow anesthesia plane (1.5% to 2% isoflurane). Best practice is to apply eye drops to mice 15 min prior to anesthesia, then keep the mice in cages in darkness to facilitate mydriasis. Second, care must be taken to avoid cataracts. During anesthesia, immediately apply eye drops with gel-like strength. Regular strength eye drops are not viscous enough to hydrate the cornea long. We do not recommend ophthalmic ointments because they appear opaque. Gel drops must be applied to both eyes and monitored frequently every 2 min. If a cataract occurs, retry imaging within 6 hours. Best practice to prevent cataract is that after eye gel is applied, a lens is placed on top of the eye to keep the moisture.³⁸ We used a plano-concave lens (LC2969, Thorlabs, Newton, New Jersey, United States) for this purpose. Furthermore, mice should be kept warm and insulated to prevent cataracts. When positioning the mouse's eyes for imaging, make sure to rotate the mouse so that the pupil appears as a circle on the viewing camera. This angle produces the best view for the retinal structure. With proper preparation, retinal imaging is quick to perform.

However, this method has limitations. Adding optical components, such as beam splitters, reduces the light reaching each sensor, which is a concern for retinal imaging where low illumination and fast acquisition are critical to prevent eye damage and motion artifacts. We used a 70-30 beam splitter to divide light between the HSI and RGB cameras, but future designs could explore more optimal configurations. The study established preliminary results on one sample. However, future studies can demonstrate replications of multiple animals. Training the pansharpening network required a customized dataset captured with our snapshot camera, underscoring the need for researchers to develop specific datasets for biological tissues. Currently, there is no research examining whether pansharpening networks trained on satellite imagery can be effectively transferred to medical imaging tasks, presenting a promising avenue for future investigation.

This hyperspectral imaging method shows potential for application to human retinas. Unlike imaging in small mammals, integrating pansharpening with modern fundus cameras for human use is straightforward due to the availability of compatible systems and extensive literature on the optical properties of the human eye. These resources could facilitate more accurate modeling of the eye's magnification factors. By producing high-resolution hyperspectral images of retinal microvasculature, this noninvasive imaging technique, when applied to humans can potentially enhance diagnostic capabilities.

Disclosures

The authors have no relevant financial interests in this article and no potential conflicts of interest to disclose.

Code and Data Availability

Code and data underlying the results presented in this paper are not publicly available at this time but may be obtained from the authors upon reasonable request.

Acknowledgments

Research reported in this publication was supported in part by the National Cancer Institute of the National Institutes of Health under Award Number R01CA288379, the Cancer Prevention and Research Institute of Texas (CPRIT) under Award Numbers RP240289 and RP240542, and the Eugene McDermott Graduate Fellowship 202009 at the University of Texas at Dallas. The manuscript is an expansion of our SPIE Proceedings paper (Tran et al., "A dual-camera high-resolution hyperspectral imaging system for the retina," doi 10.1117/12.3047906). The content

is solely the responsibility of the authors and does not necessarily represent the official views of the National Institutes of Health.

References

1. G. Lu and B. Fei, "Medical hyperspectral imaging: a review," *J. Biomed. Opt.* **19**(1), 010901 (2014).
2. B. Khoobehi, J. M. Beach, and H. Kawano, "Hyperspectral imaging for measurement of oxygen saturation in the optic nerve head," *Invest. Ophthalmol. Vis. Sci.* **45**(5), 1464–1472 (2004).
3. M. H. Tran and B. Fei, "Compact and ultracompact spectral imagers: technology and applications in biomedical imaging," *J. Biomed. Opt.* **28**(4), 040901 (2023).
4. A. London, I. Benhar, and M. Schwartz, "The retina as a window to the brain—from eye research to CNS disorders," *Nat. Rev. Neurol.* **9**(1), 44–53 (2013).
5. A. García-Llorca, H. Reynisson, and T. Eysteinnsson, "Measuring retinal vessel diameter from mouse fluorescence angiography images," *JoVE* (195), e64964 (2023).
6. M. Vandenabeele et al., "The AppNL-G-F mouse retina is a site for preclinical Alzheimer's disease diagnosis and research," *Acta Neuropathol. Commun.* **9**(1), 6 (2021).
7. Q. Li et al., "New microscopic pushbroom hyperspectral imaging system for application in diabetic retinopathy research," *J. Biomed. Opt.* **12**(6), 064011 (2007).
8. H. Y. Yao et al., "Hyperspectral ophthalmoscope images for the diagnosis of diabetic retinopathy stage," *J. Clin. Med.* **9**(6), 1613 (2020).
9. N. Lee et al., "In vivo snapshot hyperspectral image analysis of age-related macular degeneration," in *Annu. Int. Conf. of the IEEE Eng. in Med. and Biol.*, pp. 5363–5366 (2010).
10. G. Vivone et al., "A critical comparison among pansharpening algorithms," *IEEE Trans. Geosci. Remote Sens.* **53**(5), 2565–2586 (2015).
11. G. Masi et al., "Pansharpening by convolutional neural networks," *Remote Sens.* **8**(7), 594 (2016).
12. J. Ma et al., "Pan-GAN: an unsupervised pan-sharpening method for remote sensing image fusion," *Inform. Fusion* **62**, 110–120 (2020).
13. L. Ma et al., "Unsupervised super-resolution reconstruction of hyperspectral histology images for whole-slide imaging," *J. Biomed. Opt.* **27**(5), 056502 (2022).
14. M. Paques et al., "Panretinal, high-resolution color photography of the mouse fundus," *Invest. Ophthalmol. Vis. Sci.* **48**(6), 2769–2774 (2007).
15. A. Schejter et al., "Cellular resolution panretinal imaging of optogenetic probes using a simple funduscope," *Transl. Vision Sci. Technol.* **1**(2), 4 (2012).
16. S. Lemmens et al., "Combination of snapshot hyperspectral retinal imaging and optical coherence tomography to identify Alzheimer's disease patients," *Alzheimers Res. Ther.* **12**(1), 144 (2020).
17. Y. Geng et al., "Optical properties of the mouse eye," *Biomed. Opt. Express* **2**(4), 717–738 (2011).
18. K. Pruitt et al., "Design and validation of a high-speed hyperspectral laparoscopic imaging system," *J. Biomed. Opt.* **29**(9), 093506 (2024).
19. K. Pruitt et al., *A High-speed Hyperspectral Laparoscopic Imaging System*, SPIE Press, Bellingham, Washington (2023).
20. S. S. More, J. M. Beach, and R. Vince, "Early detection of amyloidopathy in Alzheimer's mice by hyperspectral endoscopy," *Investig. Ophthalmol. Vis. Sci.* **57**(7), 3231–3238 (2016).
21. T. M. Tu et al., "A new look at IHS-like image fusion methods," *Inform. Fusion* **2**(3), 177–186 (2001).
22. K. Amolins, Y. Zhang, and P. Dare, "Wavelet based image fusion techniques — an introduction, review and comparison," *ISPRS J. Photogramm. Remote Sens.* **62**(4), 249–263 (2007).
23. Q. Liu et al., "PSGAN: a generative adversarial network for remote sensing image pan-sharpening," *IEEE Trans. Geosci. Remote Sens.* **59**(2), 10227–10242 (2021).
24. F. Dadrass Javan et al., "A review of image fusion techniques for pan-sharpening of high-resolution satellite imagery," *ISPRS J. Photogramm. Remote Sens.* **171**, 101–117 (2021).
25. A. Chakrabarti and T. Zickler, "Statistics of real-world hyperspectral images," in *CVPR*, pp. 193–200 (2011).
26. F. Yasuma et al., "Generalized assorted pixel camera: postcapture control of resolution, dynamic range, and spectrum," *IEEE Trans. Image Process.* **19**(9), 2241–2253 (2010).
27. C. A. Schneider, W. S. Rasband, and K. W. Eliceiri, "NIH image to ImageJ: 25 years of image analysis," *Nat. Methods* **9**(7), 671–675 (2012).
28. Z. Hosseinaee et al., "In vivo functional and structural retinal imaging using multiwavelength photoacoustic remote sensing microscopy," *Sci. Rep.* **12**(1), 4562 (2022).
29. J. Kaluzny et al., "Bayer filter snapshot hyperspectral fundus camera for human retinal imaging," *Curr. Eye Res.* **42**(4), 629–635 (2017).
30. K. Briely-Sabo and A. Bjornerud, "Accurate de-oxygenation of ex vivo whole blood using sodium Dithionite," in *Proc. Int. Soc. Mag. Reson. Med.*, Vol. **2025** (2000).
31. S. Prahl, "Optical absorption of hemoglobin," Oregon Medical Center News (1999).

32. O. B. Olafsdottir et al., “Retinal vessel oxygen saturation during 100% oxygen breathing in healthy individuals,” *PLoS One* **10**(6), e0128780 (2015).
33. L. Ma et al., “Automatic detection of head and neck squamous cell carcinoma on histologic slides using hyperspectral microscopic imaging,” *J. Biomed. Opt.* **27**(4), 046501 (2022).
34. A. Joseph, A. Guevara-Torres, and J. Schallek, “Imaging single-cell blood flow in the smallest to largest vessels in the living retina,” *Elife* **8**, 45077 (2019).
35. L. Ma, K. Pruitt, and B. Fei, “A hyperspectral surgical microscope with super-resolution reconstruction for intraoperative image guidance,” *Proc. SPIE* **12930Z**, 129300Z (2024).
36. L. Ma, K. Pruitt, and B. Fei, “Dual-camera laparoscopic imaging with super-resolution reconstruction for intraoperative hyperspectral image guidance,” *Proc. SPIE* **12928I**, 129280I (2024).
37. D. K. Mojumder, “Muscarinic receptor antagonist and an alpha-adrenergic agonist are required in combination to provide stable mydriasis following intravitreal injection in mice,” *Biol. Med.* **2**(1), 17–23 (2010).
38. W. Ikeda, T. Nakatani, and A. Uemura, “Cataract-preventing contact lens for in vivo imaging of mouse retina,” *BioTechniques* **65**(2), 101–104 (2018).

Minh H. Tran is a PhD candidate in bioengineering at the University of Texas at Dallas. He is a graduate research assistant in the Quantitative Bioimaging Laboratory (QBIL) in the Department of Bioengineering at the University of Texas at Dallas and a student member of SPIE.

Kelden Pruitt was a research assistant in the Quantitative Bioimaging Laboratory (QBIL) and received his BS and PhD degrees in bioengineering at the University of Texas at Dallas.

Michelle Bryarly is a research assistant in the Quantitative Bioimaging Laboratory (QBIL) in the Department of Bioengineering at the University of Texas at Dallas.

Isioma Emordi is a research assistant in the Quantitative Bioimaging Laboratory (QBIL) in the Department of Bioengineering at the University of Texas at Dallas.

Arrsh Ali is a research assistant in the Quantitative Bioimaging Laboratory (QBIL) in the Department of Bioengineering at the University of Texas at Dallas.

Ling Ma is a research associate in the Department of Bioengineering at The University of Texas at Dallas. She received her BS degree in Measuring and Controlling Technology and Instruments and her PhD in Instrument Science and Technology from Tianjin University in 2015 and 2022, respectively. Her current research interests include *in vivo* HSI and hyperspectral microscopic imaging for head and neck cancer detection. She is a member of SPIE.

Baowei Fei is the Cecil H. and Ida Green Chair in systems biology science, professor of bioengineering at the University of Texas at Dallas, and professor of radiology at UT Southwest Medical Center. He is the director of the Quantitative BioImaging Laboratory (www.fei-lab.org). He is the director of the Center for Imaging and Surgical Innovation at the University of Texas at Dallas and UT Southwestern Medical Center. He is a fellow of the International Society for Optics and Photonics and a fellow of the American Institute for Medical and Biological Engineering.